Wheel Slippage and Sinkage Detection for Planetary Rovers

Giulio Reina, Lauro Ojeda, Annalisa Milella, and Johann Borenstein, *Senior Member, IEEE*

Abstract—Mobile robots are increasingly being used in high-risk rough terrain situations, such as planetary exploration and military applications. Current control and localization algorithms are not well suited to rough terrain, since they generally do not consider the physical characteristics of the vehicle and its environment. Little attention has been devoted to the study of the dynamic effects occurring at the wheel–terrain interface, such as slip and sinkage. These effects compromise odometry accuracy, traction performance, and may even result in entrapment and consequent mission failure. This paper describes methods for wheel slippage and sinkage detection aiming at improving vehicle mobility on soft sandy terrain. Novel measures for wheel slip detection are presented based on observing different onboard sensor modalities and defining deterministic conditions that indicate vehicle slippage. An innovative vision-based algorithm for wheel sinkage estimation is discussed based on edge detection strategy. Experimental results, obtained with a Mars rover-type robot operating in high-slippage sandy environments and with a wheel sinkage testbed, are presented to validate our approach. It is shown that these techniques are effective in detecting wheel slip and sinkage.

Index Terms—Rough-terrain mobile robotics, slip and sinkage detection.

I. INTRODUCTION

FOR mobile robots driving across soft soils, such as sand, loose dirt, or snow, it is critical that dynamic effects occurring at the wheel-terrain interface be taken into account. The most prevalent of these effects are wheel slip and sinkage, which greatly affect a robot's mobility. Current control and localization algorithms generally do not consider the physical characteristics of the vehicle and of its environment. Failure to understand these characteristics could lead to poor position estimation, poor traction, and possibly even to complete immobility. Field trials performed at the Jet Propulsion Lab (JPL) in Pasadena, CA, using a terrestrial analog of the Mars Exploration Rovers have indicated that there is a great amount of slippage in the drive wheels during traversal of Mars-like terrain [1]. This precludes the use of conventional dead-reckoning techniques for navigation [2]–[4], since they are based on the assumptions that wheel revolutions can be translated into linear displacement relative to

G. Reina is with the Department of Innovation Engineering, University of Lecce, Lecce, 73100 Italy (e-mail: giulio.reina@unile.it).

L. Ojeda and J. Borenstein are with the Advanced Technologies Laboratory, University of Michigan, Ann Arbor, MI 48108 USA (e-mail: lojeda@umich.edu; johannb@umich.edu).

A. Milella is with the Department of Mechanical and Management Engineering, Politecnico of Bari, Bari, Italy (e-mail: milella@poliba.it).

the ground. If one wheel slips, then the associated encoder will register wheel revolutions even though these revolutions do not correspond to a linear displacement of the wheel. Conversely, if one wheel skids, fewer encoder pulses will be produced. Thus, in order to function properly on sandy terrain, it is necessary to take into account vehicle–terrain dynamic effects such as slip and skid. Minimizing slippage not only limits odometric errors but also reduces the overall energy consumption and increases the robot's traction and climbing performance [5].

Wheel sinkage is a key variable in estimating vehicle–terrain interaction. Wheels can sink in soft soils to depths sufficient to prohibit further motion. As is the case with wheel slippage, it is desirable to have the capability to sense excessive wheel sinkage so that corrective controls may be executed before the vehicle becomes immobile 0. Sinkage measurements are also valuable for reducing position estimation errors. The accuracy of kinematic models used to estimate rover position updates depends on accurate knowledge of the wheel radius, which is used to compute the equivalent linear distance traveled by a wheel from the encoder reading. As the load-bearing strength of soil varies under rover wheels, so does the amount of wheel sinkage and the wheel effective rolling radius; thus, decreasing the odometric accuracy. To reduce the effect of propagating this nonsystematic error during rover traverses on varied terrain, a means to measure wheel sinkage (and therefore effective wheel radius) is needed. Finally, wheel sinkage has been shown to be an important input to terrain identification according to classical terramechanics theory [7].

This paper presents recent work of the authors in algorithm development for the study of the ill-effects associated with the interaction of vehicle wheels with soft sandy terrain. Novel measures for wheel slippage detection are introduced based on observing many different sensor modalities implemented on the vehicle and defining deterministic conditions for slippage occurrences. Specifically, three methods are described that compare data from encoders with each other, gyro data, and electric motor current data to determine whether wheels are slipping or "gripping" in a given sampling interval.

Current research in the field aims at detecting slippage using either exteroceptive or absolute sensors, or both. Helmick *et al.* [8] proposed a system for detecting slippage in a Mars rover based on fusing visual odometry and inertial measurements through a Kalman filter pose estimator. Baumgartner *et al.* [4] utilized a sun sensor to improve rover state estimates. Combination of visual odometry with an absolute heading sensor, such as a compass or sun sensor, was shown to be effective for robust long-range navigation [6]. In contrast to these methods, the approach described in this paper relies on purely proprioceptive sensors.

Fig. 1.   Rover Fluffy.

Fig. 2.   Nomenclature for wheel velocities in the rover Fluffy.

An innovative visual sinkage estimation (VSE) algorithm is also presented. This module assumes the presence of a camera mounted on the vehicle body, with a field of view containing the wheel–terrain interface. A pattern of equally spaced concentric black circumferences on a white background is attached to the wheel in order to determine the contact angle with the terrain using an edge detection-based strategy.

In research with a similar focus, Iagnemma *et al.* [9] described an online visual sinkage estimation algorithm that relied on the analysis of grayscale intensity along the wheel rim. Assuming that the wheel has a different color than the terrain, the location of the terrain interface is computed as the point of maximum change in intensity. This method is relatively simple and computationally efficient, but it is very sensitive to lighting variations and shadows. Moreover, it is based on the assumption that the wheel has a different gray level than the terrain, which implies previous knowledge of the soil appearance characteristics. Conversely, our method does not require any *a priori* information about the environment, while preserving computational efficiency.

The methods proposed here provide a means for detecting and possibly even estimating the ill-effects of wheel–terrain interaction on sandy soft terrain. Such techniques can enhance vehicle safety and mobility through integration with localization, control, and planning methods.

One limitation of our approach is that it can detect slippage along the longitudinal direction of motion only. However, in the presence of lateral forces, the wheels move at an angle (slip angle) with respect to the longitudinal wheel plane, resulting in lateral slippage [10]. This problem is not addressed in this work.

The wheel slippage detection algorithms were extensively tested on a fully functional kinematically equivalent clone of JPL's Fido-class rovers [11], which was built at the Mobile Robotics Laboratory, University of Michigan. Our clone, named Fluffy (see Fig. 1), is about half the size of Fido, but it features the same six-wheel independent drive steering and a rocker-bogie passive suspension system. Fluffy is equipped with an onboard in-house built inertial measurement unit (IMU) that uses three fiber optic gyros for estimating the spatial orientation of the robot, two accelerometers for static tilt measurements, and six independent wheel encoders for odometry.
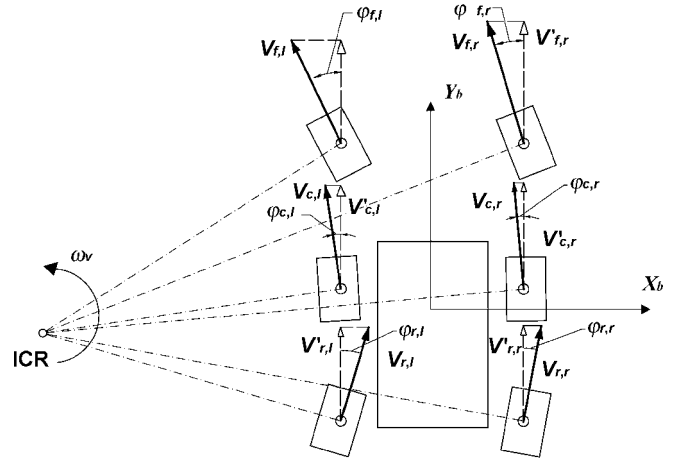
Section II introduces measures for wheel slippage detection. The test bed for wheel sinkage identification, built at the Politecnico of Bari, as well as the vision-based algorithm for sinkage estimation are described in Section III. Experimental results and a discussion conclude this paper in Section IV.

II. Measures for Wheel Slippage Detection

The greatest enemy of odometric accuracy is wheel-slippage, and vehicles that travel on sandy soils are at risk the most. This is particularly true for rover-like vehicles due to their overconstrained nature, i.e., having more independent motors than degrees of freedom of motion. For these vehicles, any momentary mismatch between wheel velocities with respect to the vehicle kinematic constraints will result in wheels "fighting" each other, and, consequently, slippage with ill-effects such as position estimation errors, increased power consumption, and loss of traction.

In earlier work, we proposed an odometry method that could provide good travel distance estimates as long as at least one wheel was gripping (=the opposite of "slipping") [12]. However, on soft sandy terrain, all the robot's wheels are likely to slip simultaneously. We refer to this condition as all-wheel-slippage (AWS).[1]

In this section, we discuss methods for the detection of AWS conditions. The rationale is that it is generally beneficial to know that AWS has occurred or that the wheel is approaching a condition of impending slippage to reduce and compensate odometry errors and optimize traction control [2], [17]. In order to detect AWS, we developed a set of what we call AWS indicators. The general approach is based on observing many different onboard sensor modalities and defining deterministic conditions for wheel slippage. The output of an AWS indica-

[1]Because of ambiguity in the way the terms slip and skid are used in the scientific literature, we define these terms in the context of this paper as follows: "Slip" or "slipping" is the loss of traction that results when the motor applies too much power to the wheel, e.g., over acceleration. "Skid" or "skidding" is the loss of traction that results when the vehicle is in motion but a wheel is blocked or partially blocked from rolling by excessive friction in the drive train or the effect of motor braking. We refer to slip and skid collectively as "Slippage."
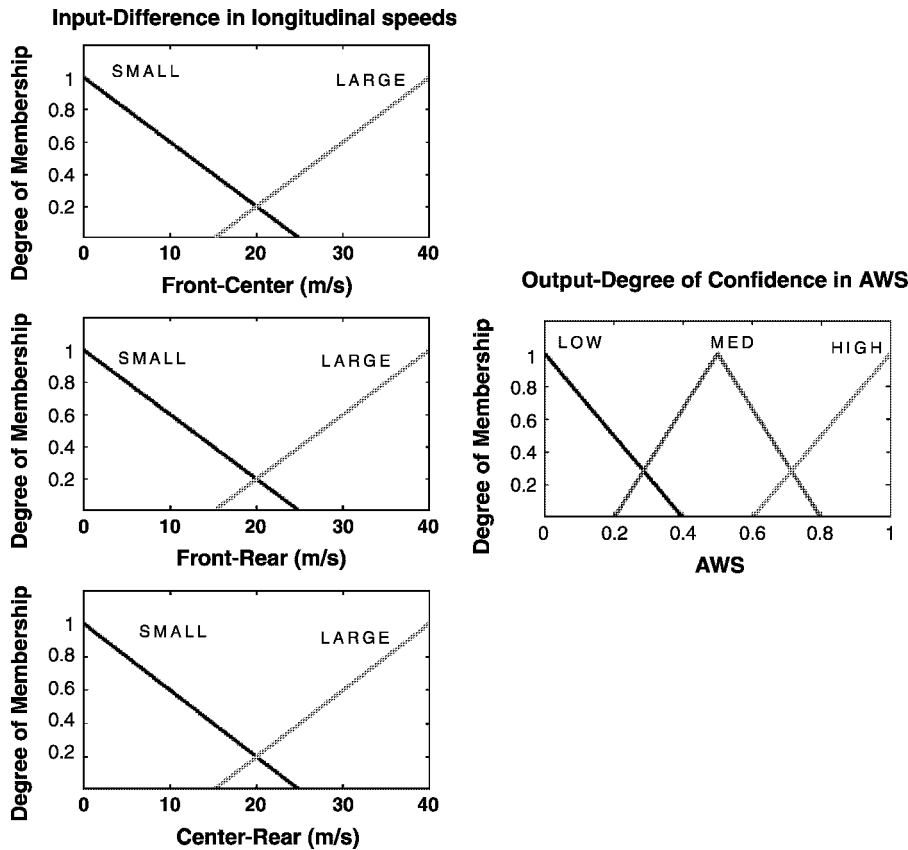
Fig. 3. Membership functions of the fuzzy fusion for the EI.

tor can be a binary flag that indicates that AWS has occurred or it can be a fuzzy quantity that expresses our certainty that AWS occurred. Fuzzified outputs from multiple indicators can be combined through fuzzy logic.

The most effective AWS indicators we found are as follows:
1) *Encoder Indicator* (EI)—compares encoder readings with each other.
2) *Gyro Indicator* (GI)—compares encoder readings with those of the z-axis gyro.
3) *Current Indicator* (CI)—monitors motor currents, which are roughly proportional to the external torque applied to each wheel.

In the remainder of this section, we discuss each indicator in some detail and offer experimental results in Section IV.

A. Encoder Indicator

Fig. 2 shows a schematic diagram of our rover Fluffy. A coordinate system is attached to the vehicle so that the y-axis of the vehicle coordinate system is aligned with the vehicle's longitudinal direction. Each wheel i, j has a linear velocity vector $V_{i,j}$ and a steering angle $\varphi_{i,j}$ (index i = front, center, or rear, and index j = left or right). $\varphi_{i,j}$ is measured between the longitudinal direction of the vehicle Y_b and the steering direction of the wheel. The projection of the linear velocity vector $V_{i,j}$ onto the y-axis is called longitudinal velocity component $V'_{i,j}$. While the linear velocities of the wheels differ from each other

according to their distance from the instantaneous center of rotation (ICR) of the vehicle, their longitudinal components must be equal on either side of the vehicle [13].

Our hypothesis is that unequal longitudinal velocity components in the three wheels of a side suggest wheel slippage. In order to express this hypothesis, we adopted fuzzy logic that uses rules to map from inputs to outputs [14]. The triangular membership functions used in our system, i.e., the curves that map each point in the input space to a membership value or grade between zero and one, are shown in Fig. 3. The fuzzy data fusion uses three inputs and one output. Inputs are the sensory data, i.e., the differences in longitudinal velocity components between the front and the center wheel, the front and the rear wheel, and the center and the rear wheel, respectively. The output is a dimensionless factor ranging from zero to one that expresses the degree of confidence we that AWS has occurred.

The fuzzy inference system fuses the sensory information based on the *if–then* rule set shown in Table I. Those rules express our physical understanding of the behavior of the encoders and they were chosen to give the best performance over other alternatives using a trial and error process. The rule set is not unique; new rules may be thought and implemented to improve the output of the system.

Note that the influence of the front wheel encoder is smaller than that of the center and the rear encoder due to the disproportionally small load acting on the front axle of Fluffy (the same is true for JPL's Fido).

TABLE I
FUZZY LOGIC RULES FOR THE ENCODER INDICATOR

Rule #	Input: Difference in longitudinal speeds between			Output: Confidence in AWS (low = vehicle gripping; high = vehicle slipping)
	Front–Center	Front–Rear	Center–Rear	
1	Small	Small	Small	Low
2	Small	Small	Large	High
3	Small	Large	Small	Med.
4	Small	Large	Large	High
5	Large	Small	Small	Low
6	Large	Small	Large	Med.
7	Large	Large	Small	Med.
8	Large	Large	Large	High

TABLE II
FUZZY LOGIC RULES FOR THE GYRO INDICATOR

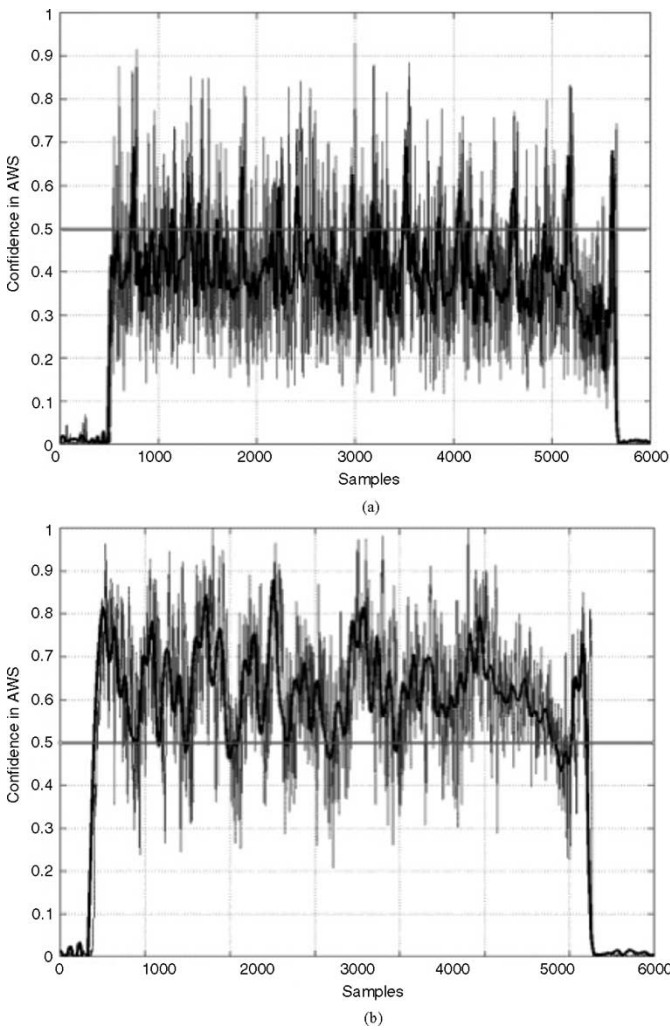| Rule #	Input: $\omega_{\mathrm{Enc},i} - \omega_{\mathrm{Gyro}}$			Output: Confidence in AWS (low = vehicle gripping; high = wheel slipping)
	Front	Center	Rear	Front
1	Small	Small	Small	Low
2	Small	Small	Large	Med.
3	Small	Large	Small	Med.
4	Small	Large	Large	High
5	Large	Small	Small	Small
6	Large	Small	Large	High
7	Large	Large	Small	High
8	Large	Large	Large	High

Fig. 4. Output of the Fuzzified Encoder Indicator for different terrains (gray line). The bold black line shows the smoothed output. (a) High-traction terrain, no slippage. The AWS flag was raised 23% of the time. (b) Sloped sandy terrain causing lots of slippage. The AWS flag was raised 82% of the time. The binary AWS flag is raised whenever the output is greater than 0.5.

Table I must be applied for both the right and the left side of the rover. Fig. 4 shows the output of the fuzzy logic system of the EI for (a) a high-traction and (b) a high-slippage terrain.

B. Gyro Indicator

This method aims at detecting wheel slippage by comparing encoder data with gyro data. The motion of a rigid body can always be expressed as a momentary pure rotation about the ICR, as shown in Fig. 2. For straight-line motion, the distance from the ICR to each wheel is of infinite length.

We can compute the rate-of-turn ω of the vehicle from each one of the encoder pair i (index i = front, center, and rear), according to

$$\omega_{\mathrm{Enc},i} = \frac{d_{i,r}\cos\varphi_{i,r} - d_{i,l}\cos\varphi_{i,l}}{bT}. \qquad (1)$$

where
- $d_{i,r/l}$ distance traveled by the right/left wheel of wheel pair i;
- $\varphi_{i,r/l}$ steering angle of the right/left wheel of wheel pair i;
- b vehicle width (distance between the left and right wheel);
- T sampling interval.

We can now compare each of the three $\omega_{\mathrm{Enc},i}$ with the rate-of-turn measured by the z-axis gyro ω_{Gyro}, which we consider the ground truth in this approach. If no slippage occurred in a wheel pair, then one can expect good correspondence between the rate-of-turn derived from the encoders of that wheel pair and the gyro. Poor correspondence suggests wheel slippage.

Also for the GI, we developed a fuzzy inference system to fuse sensory data. Table II shows the fusion rules that translate our knowledge base of the behavior of the sensors. The membership functions used as input and output of the fuzzy system are similar to those described above for the EI. Fig. 5 shows the output of the fuzzy logic system of the GI for a test where the rover was commanded to travel with a constant rate-of-turn of $4°/s$ on sand. During the run, the wheels were deliberately forced to slip by manually holding back the vehicle using strings attached to its frame. The bold black line is the ground truth provided by the gyro. The black, dotted gray, and gray lines are the rates-of-turn estimated by the front, center, and rear encoder pairs, respectively. The output of the GI is expressed in terms of a binary state, which we refer to as an AWS flag. The AWS flag is raised whenever the system's confidence in the existence of an AWS condition, as estimated by the fuzzy fusion system, is
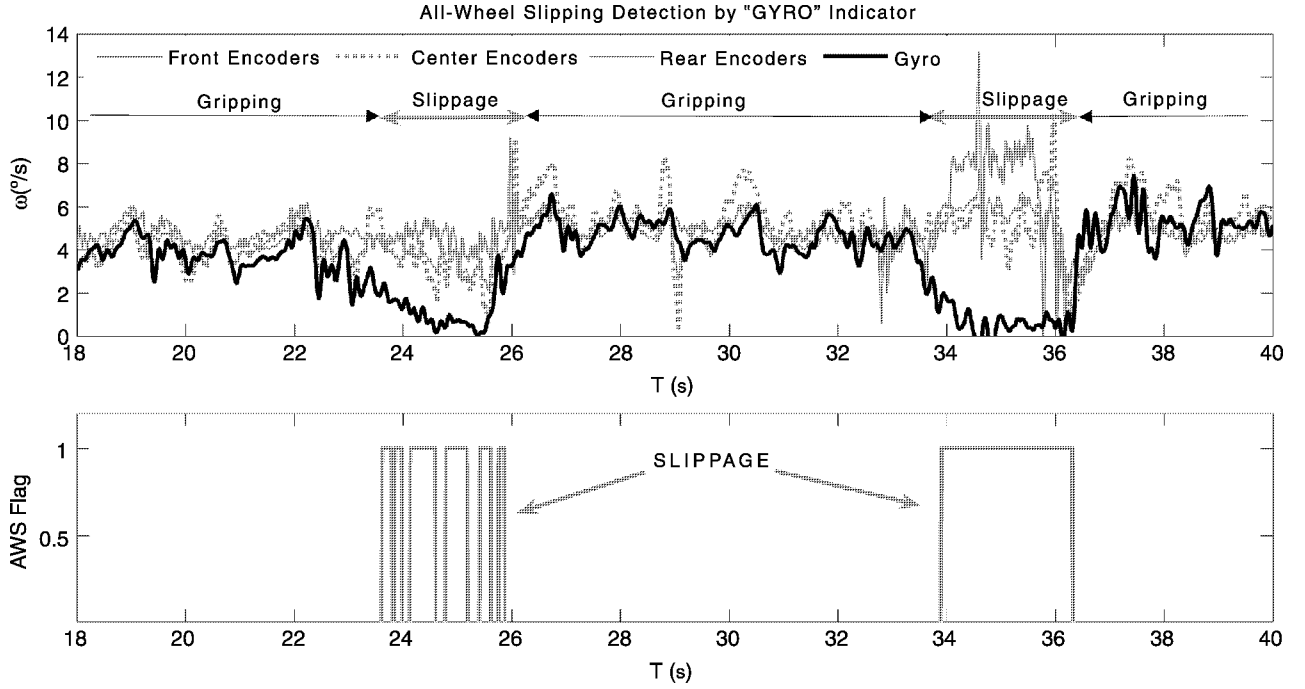
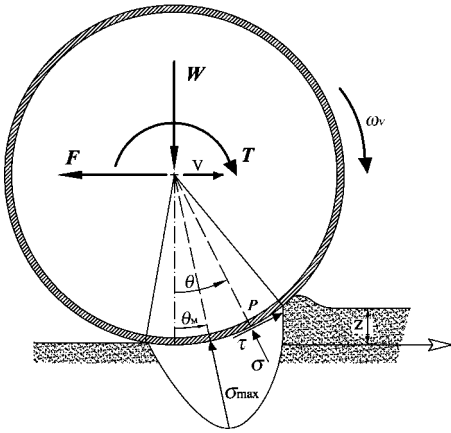Fig. 5.   Effectiveness of the Gyro Indicator.

Fig. 6.   Wheel–soil interaction model (adapted from [15]).

greater than 0.5. This is shown by a gray line in the bottom part of Fig. 5.

C. Current Indicator

The CI aims at detecting AWS through the use of the well-established physical model of wheel–terrain interaction mechanics. The interaction between wheel and terrain has been shown to play a critical role in rough terrain mobility [15]. When a torque is applied to the wheel, shearing action is initiated at the wheel–terrain interface creating a force F, which is used to propel the vehicle and overcome the rolling resistance (see Fig. 6). F is usually referred to as the tractive effort. The maximum tractive effort that can be developed by a wheel is determined by the shear strength of the terrain according to the

Coulomb–Mohr soil failure criterion [16]

$$F_{\text{Max}} = A \cdot (c + \sigma \cdot \tan\varphi) = A \cdot c + W \cdot \tan\varphi \qquad (2)$$

where

c, φ cohesion and internal friction angle, respectively. These coefficients characterize the behavior of the terrain;

A wheel contact patch, which is a function of wheel geometry and of the vertical load acting on the wheel;

σ normal component of the stress region at the wheel–terrain interface (Fig. 6);

W vertical load acting on the wheel.

Since torque is proportional to current, the knowledge of the maximum allowable shear strength of a given terrain allows estimation of the electrical current $I_{\max}$ that is drawn by the wheel drive motor corresponding to the maximum tractive effort. We call this current the *maximum traction current*. In practice, $I_{\max}$ can be determined experimentally for a given terrain, and the condition of total slippage (100%) of the wheel is evaluated as

$$|I_{\max} - I_i| \leq \Delta I \qquad (3)$$

where I_i is the current drawn by the motor of wheel i and ΔI is an empirically determined threshold (in our system: 10% of $I_{\max}$). We should note that $I_{\max}$ is a function of the vertical load acting on the wheel for a given terrain. For example, when the vehicle is traversing a slope, $I_{\max}$ will decrease since less of its weight acts as a force normal to the surface. We account for this fact by increasing ΔI (thus lowering the current threshold that suggests slippage) by an empirically determined factor C_θ. Therefore, (3) can be rewritten as

$$|I_{\max} - I_i| \leq \Delta I + C_\theta \cdot \theta_{\text{r}} \qquad (4)$$

where θ_r is the rover's pitch angle as measured by the on-board IMU. The logical extension to this improvement would be adding compensation for changes in the roll angle. However, we must be careful when doing so, because changes in the roll angle may also be accompanied by lateral slippage, which cannot be corrected by our method.

We should point out that for relatively small angles the improvement resulting from pitch compensation is very small and may be omitted. This can be explained by the fact that the vertical load changes as a function of the cosine of the tilt angle; therefore, only large tilt angles would produce a significant change in (4).

It should also be noted that (4) could only be used for predicting the maximum tractive effort for a wheel. However, methods for evaluating quantitatively the amount of slippage and thus compensating for position estimation errors have been proposed by the authors in previous works where the shear stress–shear displacement relationship of a given terrain was also considered [17]. Here, we are concerned with developing a framework for different AWS indicator and for that our simplistic empiric approach is sufficient.

It should be noted that although the CI indicator requires prior knowledge of terrain parameters, it is feasible (and we have indeed done so in tests at our lab) to estimate the relevant soil parameters by performing a simple experiment in the beginning of a mission. It takes only a few minutes to perform this experiment and it can be done in real time and while traveling. Description of this method exceeds the scope of this paper; however, details are given in [18].

III. WHEEL SINKAGE ESTIMATION

In this section, we present a vision-based algorithm for estimating wheel sinkage in deformable soil, which we call visual sinkage estimation (VSE).

We assume the presence of a camera mounted on the vehicle body, with a field of view containing the wheel–terrain interface. We also assume that the location of the wheel relative to the camera is known and fixed during travel. Sinkage z can be evaluated by estimating the contact angle θ_c between wheel and terrain (Fig. 7) using the geometrical relationship

$$z = R(1 - \cos \theta_c) \qquad (5)$$

The VSE requires a pattern of equally spaced 1-mm thick concentric black circumferences on a white background attached to the wheel in order to determine θ_c using an edge detection-based strategy [19]. This approach allows algorithmic simplicity and computational efficiency, providing fast real-time measurements.

In practice, the VSE operates by identifying the wheel radial lines (radial gray lines in Fig. 7) where the number of detected edges is less than that expected when the wheel rolls without sinkage. Those lines can be associated with the part of the wheel obscured by soil and thus with the sinkage.

Specifically, the algorithm consists of the following steps: 1) region of interest (ROI) identification; 2) pixel intensity computation; and 3) contact angle estimation.
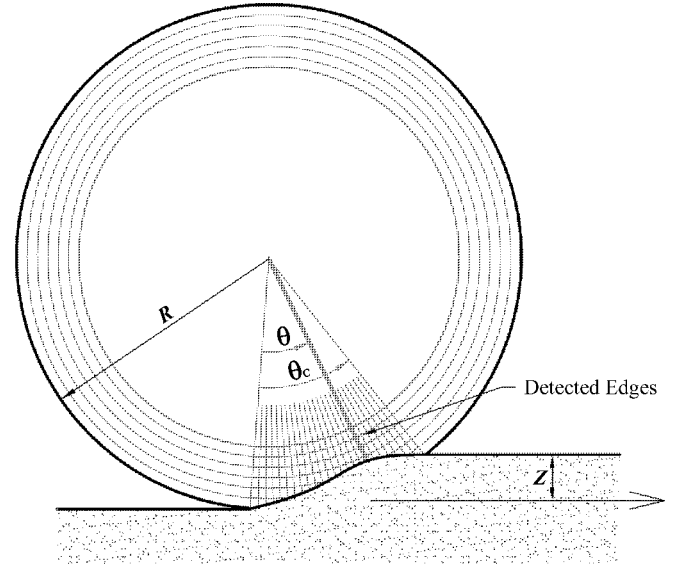

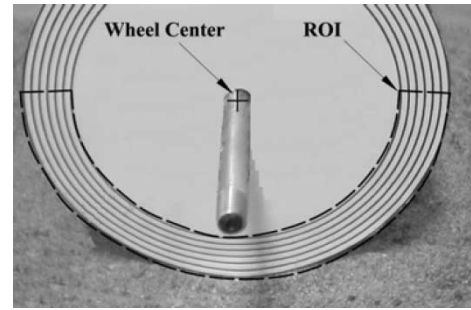Fig. 7.   Rigid wheel sinking into deformable terrain.

Fig. 8.   ROI identification for a sample image.

We now discuss each step in detail.

1) ROI Identification: In order to estimate the contact angle θ_c, the annular region along the wheel rim including the circumference pattern is the only image area that needs to be examined. Thus, a ROI identification is performed first in order to reduce computational time and improve accuracy. Given the position of the wheel center relative to the camera and the geometry of the wheel, the ROI can be detected using simple geometric projections. This is shown in Fig. 8 where the ROI is overlaid over a sample image.

2) Pixel Intensity Computation: A pixel intensity analysis is performed along radial lines spanning across the selected ROI with an angular resolution of 1°. A typical intensity plot along a radial line for a test on sand is shown in Fig. 9. The VSE differentiates between a so-called wheel region, where the wheel is not obscured by sand, and a soil region, where the soil is covering the wheel. The wheel region is characterized by high intensity variations that can be classified as edges, while the soil region shows an almost uniform intensity value. An adaptive threshold for selecting the appropriate edge intensity contrast along each radial line of inspection was experimentally determined as

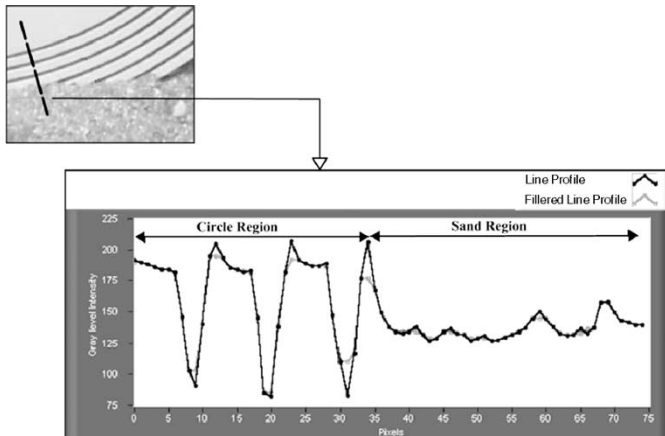$$C = \frac{L_{\mathrm{Max}} - L_{\mathrm{Min}}}{2} \qquad (6)$$

Fig. 9.   Sample plot of pixel intensity along a radial line.

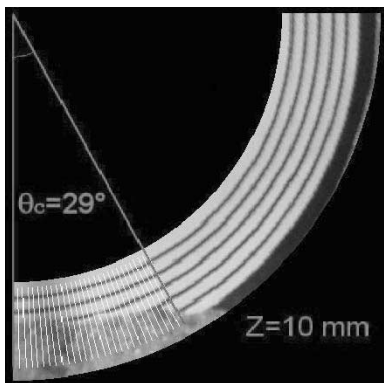Fig. 11.   Adjustable tilt platform.

Fig. 10.   Contact angle identification.

where L_{Max} and L_{Min} are the maximum and the minimum intensity measured along the given line. Filtering is applied to reduce noise and small-scale changes in intensity due to reflection, pebbles, etc.

3) Contact Angle Estimation: The contact angle θ_c is computed as the wheel angle where the transition between the wheel region and the soil region occurs. For the sample image of Fig. 10, this angle results in $\theta_c = 29°$ with a related wheel sinkage of $z = 10$ mm.

IV. EXPERIMENTAL RESULTS

In this section, we present a comprehensive set of experiments to validate our approach. The effectiveness of the AWS indicators was tested on Fluffy operating on sandy nonflat terrain. The vision-based module for sinkage estimation was experimentally examined using a single-wheel testbed.

A. AWS Indicators

As demonstrated by the Mars exploration of the NASA/JPL rover Opportunity [20], wheel slippage is a dominant disturbance on sandy slopes. For that reason, we focused on two sets of experiments. In the first set, we observed the behavior of Fluffy as it climbed a single sandy slope. In the second set,
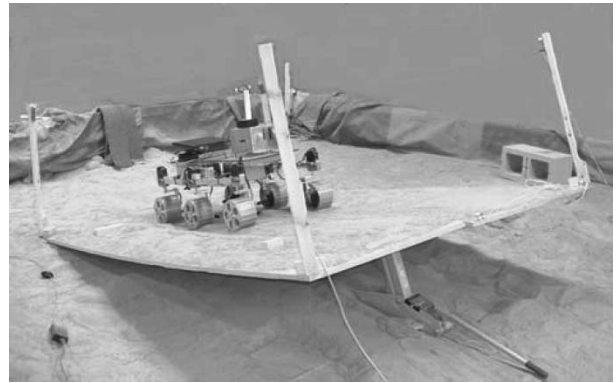
Fluffy traversed two sandy mounds. The main difference between these experiments is that in the former experiment wheel slippage is monotonous and almost constant, while in the latter experiment the robot experiences alternating and varying episodes of slippage.

1) Climbing Sandy Slopes: We performed a first set of experiments using the tilt platform shown in Fig. 11. The platform consists of a 3 m × 2 m plywood panel that can be jacked up to modify the inclination of the slope. The plywood was covered with a 2-cm-thick sand layer. Fluffy was remotely controlled to drive-up the platform with a constant speed of 6 cm/s starting from a horizontal area, about 2 m before the beginning of the slope. Different platform inclinations were tested varying from $0°$ to $17°$.

For all the experiments, the slippage detection based on the AWS indicators is expressed in terms of a binary output in the form of what we call the AWS flag. When the slippage condition established by the indicator is simultaneously met by all the wheels of the vehicle, then the AWS flag is raised. The AWS flag is lowered when at least one wheel of the vehicle is gripping.

On each of the four corner of our sandbox, we installed an ultrasonic receiver. Together with a star-like formation of four ultrasonic transmitters mounted on Fluffy, they form a ground truth position measuring system. Within the confined area of our sandbox this system provides absolute position information in real time and with subcentimeter accuracy. From this ground truth data, we can easily determine when the rover was experiencing slippage: the speed measured by the absolute position sensor is no longer equal to the nominal speed of the rover. When this condition is detected, the ground truth AWS flag is raised.

The original sensor signals and the output of the indicators are plotted in Fig. 12 for a typical run on a $12°$ slope. The upper plot shows the sensor signals used in the EI for the left side of the vehicle. The black, dotted black, and gray lines are the differences in longitudinal speed between, respectively, the front and the center, the front and the rear, and the center and the rear wheel. The output of the EI is the AWS flag shown by black dots in the bottom graph of Fig. 12.
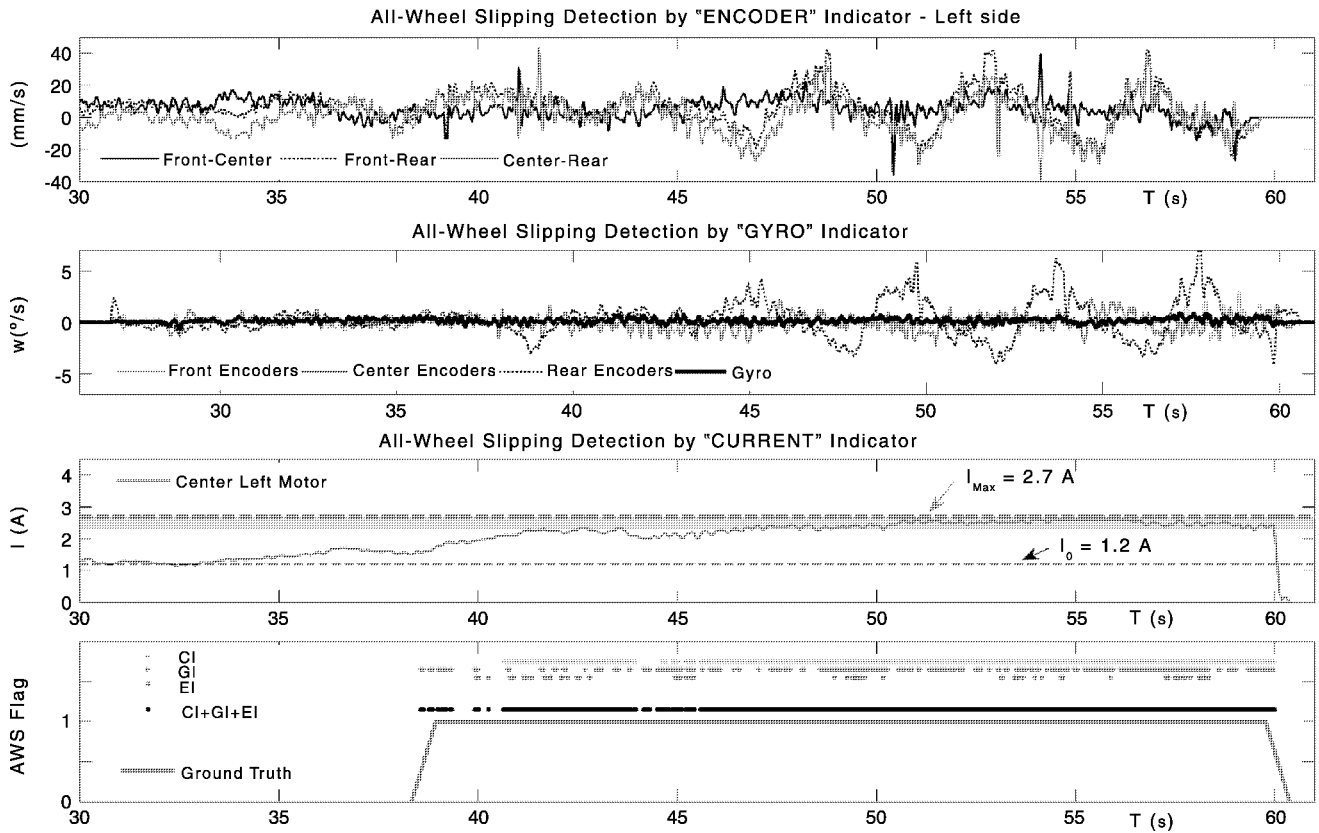
Fig. 12.   AWS detection using the EI, the CI, and the GI during the traverse of a sandy slope.

The second plot shows the sensor signals used in the GI. The bold black line is the ground truth provided by the gyro. The gray, dark gray, and dotted black lines are the rates-of-turn computed by the front, center, and rear encoder pair, respectively. The output of the GI is the AWS flag, shown by dark gray dots in the bottom graph of Fig. 12. Because many of the dots are very close to each other, they may look like a solid line.

The third plot of Fig. 12 shows the sensor signals of the CI for the left center motor. Whenever that current is within the shaded area, the condition of (4) is met and slippage of that wheel is likely. When (4) is met for all six motors, then the current-based AWS flag is raised. This flag is shown as the gray dots in the bottom graph along with the ground truth flag, which is indicated by the continuous gray line. We should explain, though, that the front wheels of Fluffy (as well as those of JPL's Fido-class rovers) carry only a disproportionly small load. For this reason, we disregard and exclude from the motor current measurements the currents of the front motors.

As the vehicle travels across the horizontal portion of the sandbox (first 38 s), no significant slippage occurs and in each drive motors flows the nominal electrical operating current I_o. The beginning of the slope marks the onset of vehicle slippage as shown by the ground truth AWS flag.

We can thus compare the accuracy of the EI, the GI, and the CI AWS flags to the ground truth flag. For this experiment, the EI correctly flagged AWS for 31%, while the GI was correct for 56% of the time. The CI flagged AWS correctly for 91% of the time.
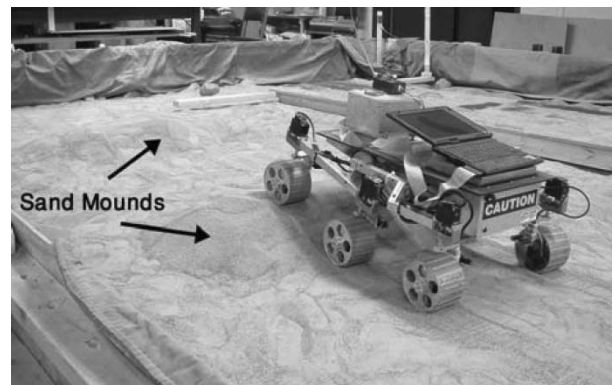

Fig. 13.   Fluffy negotiates a sand mound along a 4-m path.

When the three flags were logically OR-ed, the indicators were correct for 94% of the time. The percentage of false positives (warning of AWS when there actually was no AWS) was only 1%.

2) Traversing Sand Mounds: In this set of experiments, Fluffy was commanded to follow a 4-m straight path traversing two sand mounds at a speed of 6 cm/s, as shown in Fig. 13. The height of the mounds was about 20 cm.

The original sensor signals and the output of the indicators are plotted in Fig. 14. The upper plot shows the sensor signals used in the EI for the right side of the vehicle.
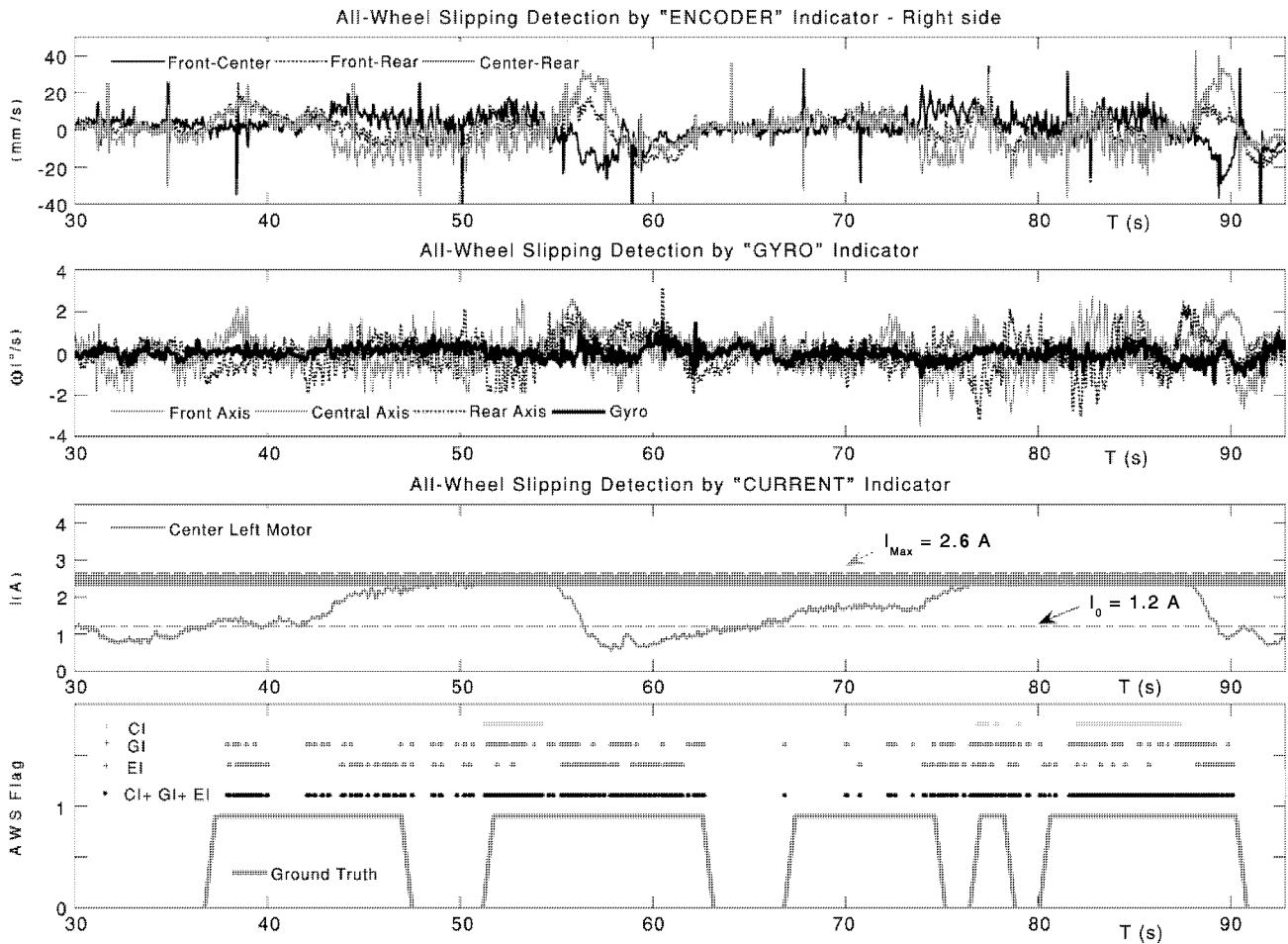
Fig. 14. Effectiveness of the EI, the GI, and the CI during the negotiation of 4-m path with two sand mounds.

The black, dotted black, and gray lines are the differences in longitudinal speed between, respectively, the front and the center, the front and the rear, and the center and the rear wheel. The output of the EI is the AWS flag shown by black dots in the bottom graph of Fig. 14. The second plot shows the sensor signals in the GI. Again, the bold black line is the ground truth for this indicator, provided by the gyro.

The gray, dark gray, and dotted black lines are the rates-of-turn as computed by the front, center, and rear encoder pairs, respectively. The output of the GI is the AWS flag shown by dark gray dots in the bottom graph of Fig. 14. The third plot shows the electrical current measured in the center left motor. When the slippage condition expressed by (4) is met for all the wheels, then the current-based AWS flag is raised. This flag is shown as the gray dots in the bottom graph.

We can compare the accuracy of the EI, the GI, and the CI AWS flags to the ground truth flag, shown by a continuous gray line in the bottom part of Fig. 14. For this experiment, we found that the EI was correct for 25% of the time whereas the GI flagged AWS correctly 38% of the time. The CI flagged AWS correctly only 18% of the time.
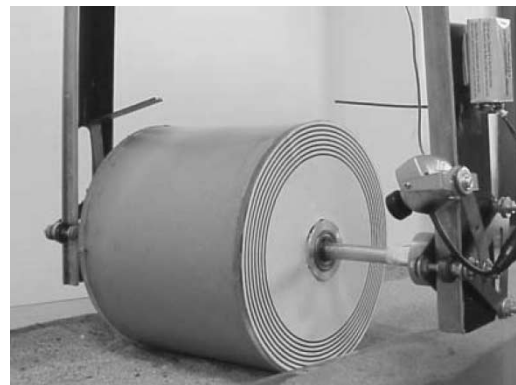

Fig. 15. Test bed for wheel sinkage estimation.

When the three flags were logically OR-ed, the indicators were correct 61% of the time. The percentage of false positives was 12%.

B. Sinkage Estimation

The performance of the VSE module was tested using the testbed shown in Fig. 15. It consists of a driven 16-cm-diameter
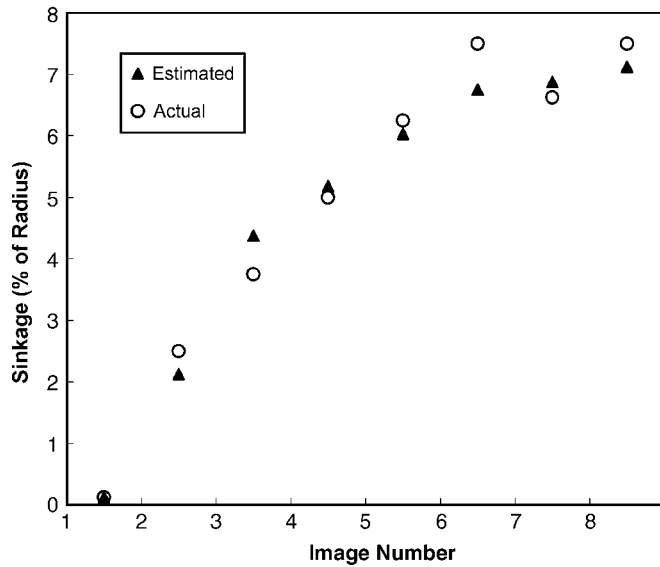
Fig. 16.   Real-time performance of the VSE.

Fig. 18.   Influence of lighting variations on the VSE.

ally, the algorithm detected wheel sinkage with reasonably good accuracy; the error E was always below 13%. No misidentification was detected in all the experiments due to reflections off the wheel and shadowing.

The relatively low accuracy of the VSE can be explained by considering that the resolution of the measuring system is bounded by the distance between the circumferences of the pattern attached to the wheel (2 mm for our case). However, better resolution may be achieved by employing a more sophisticated camera.

The algorithm also proved to be very robust to variations of lighting conditions. Representative results are shown in Fig. 18. The VSE continued to work accurately even under low-light conditions (90% less than optimal intensity, i.e., $L = 0.9$). The VSE was able to provide real-time estimation of wheel sinkage with minimum computational requirements and a sampling rate of 5 Hz.
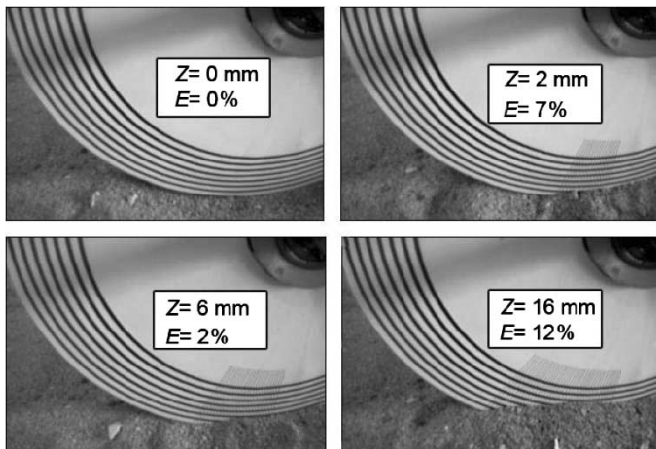

Fig. 17.   Visual estimation of wheel sinkage by the VSE.

wheel mounted on an undriven vertical axis. A low-cost wireless one-channel analog camera is attached to the wheel with a field of view containing the wheel–terrain interface. The actual sinkage of the wheel can be estimated from a potentiometer mounted on the vertical axis of the system.

Experiments were performed under different operating conditions including nonflat terrains, variable lighting conditions, and terrain with and without rocks. Fig. 16 shows representative results obtained by the VSE operating in real time for a typical run on soft sand under uniform lighting. The actual and visually measured sinkage are expressed as a percentage of the wheel radius ($R = 80$ mm). The average error was within 8% with a worst case of 15%.

Experiments were performed to test the robustness of the VSE to disturbances such as rocks, sparsely distributed across the camera field of view, and uneven lighting. Representative results are shown in Fig. 17 for a set of sample images. Gener-
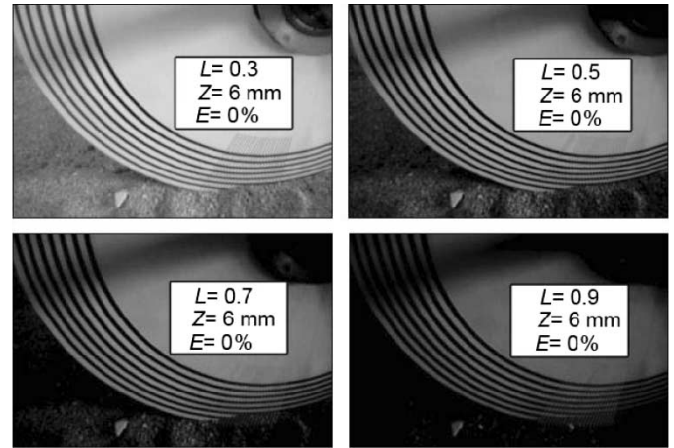
V. CONCLUSION

This paper presented methods for wheel slippage and sinkage detection, optimized for rough-terrain mobile robots.

Novel measures for wheel slippage identification were presented, which compare readings from encoders with each other, with data from a gyroscope, and with current sensors mounted on onboard the vehicle. It was shown that those methods are effective in experimental trials on sandy nonflat terrain, detecting 61%–94% of the occurrences of vehicle slippage.

An innovative vision-based algorithm for wheel sinkage estimation was also introduced and shown to be computationally efficient, relatively accurate with maximum errors below 15%, and very robust to disturbances and variations in lighting condition.

These techniques can be used to gain important information about the vehicle–terrain interaction and to improve dead-reckoning accuracy and traction control in rough-terrain autonomous vehicles.

REFERENCES

[1] T. Huntsberger *et al.*, "Rover autonomy for long range navigation and science data acquisition on planetary surfaces," presented at the *IEEE ICRA*, Washington, DC, 2002.

[2] L. Ojeda, G. Reina, and J. Borenstein, "Experimental results from FLEX-nav: An expert rule-based dead-reckoning system for mars rovers," in *Proc. IEEE Aerospace Conf.*, Big Sky, MT, 2004, pp. 816–825.

[3] Y. Fuke and E. Krotkov, "Dead reckoning for a lunar rover on uneven terrain," in *Proc. IEEE ICRA*, vol. 1, 1996, pp. 411–416.

[4] E. T. Baumgartner, H. Aghazarian, and A. Trebi-Ollennu, "Rover localization results for the FIDO rover," in *Proc. Conf. Sensor Fusion Decentralized Control Auton. Robotic Syst.*, 2001, pp. 34–44.

[5] K. Iagnemma and S. Dubowsky, "Mobile robot rough-terrain control (RTC) for planetary exploration," presented at the *ASME Biennial Mechanisms and Robotics Conf.*, Baltimore, MD, 2000.

[6] C. Olson, L. Matthies, M. Schoppers, and M. Maimone, "Robust stereo ego-motion for long distance navigation," in *Proc. IEEE Conf. Comput. Vision Pattern Recognition*, vol. 2, 2000, pp. 453–458.

[7] K. Iagnemma, S. Kang, H. Shibly, and S. Dubowsky, "Online terrain parameter estimation for wheeled mobile robots with application to planetary rovers," *IEEE Trans. Robot.*, vol. 20, no. 2, pp. 921–927, Oct. 2004.

[8] D. M. Helmick, Y. Chang, S. I. Roumeliotis, D. Clouse, and L. Matthies, "Path following using visual odometry for a mars rover in high-slip environments," presented at the *IEEE Aerospace Conf.*, Big Sky, MT, 2004.

[9] K. Iagnemma, C. Brooks, and S. Dubowsky, "Visual, tactile, and vibration-based terrain analysis for planetary rovers," presented at the *IEEE Aerospace Conf.*, Big Sky, MT, 2004.

[10] J. Wong, *Theory of Ground Vehicles*. New York: Wiley, 2001.

[11] E. Tunstel *et al.*, "FIDO rover system enhancements for high-fidelity mission simulations," in *Proc. IAS-7*, Marina del Rey, CA, 2002, pp. 349–356.

[12] L. Ojeda and J. Borenstein, "Methods for the reduction of odometry errors in over-constrained mobile robots," *Auton. Robots*, vol. 16, pp. 273–286, 2004.

[13] G. Reina "Rough terrain mobile robot localization and traversability with applications to planetary explorations," Ph.D. thesis, Politecnico di Bari, Bari, Italy, 2004.

[14] J. S. Jang, C. T. Sung, and E. Mizutani, *Neuro-fuzzy and Soft Computing: A Computational Approach to Learning and Machine Intelligence*. Upper Saddle River, NJ, Matlab Curriculum Series, Prentice-Hall, 1997.

[15] G. Bekker, *Introduction to Terrain-Vehicle Systems*. Ann Arbor: Univ. Michigan Press, 1969.

[16] ——, *Off the Road Locomotion*. Ann Arbor: Univ. Michigan Press, 1960.

[17] L. Ojeda, G. Reina, D. Cruz, and J. Borenstein, "The FLEXnav precision dead-reckoning system," in *Int. J. Vehicle Auton. Syst.*, to be published.

[18] L. Ojeda, J. Borenstein, and G. Witus, "Terrain trafficability characterization with a mobile robot," presented at the *7th SPIE Defense and Security Conf.*, Orlando, FL: Unmanned Ground Vehicle Technology, Mar. 28–Apr. 1, 2005.

[19] R. M. Haralick and L. G. Shapiro, *Comput. Robot Vision*. Reading, MA: Addison-Wesley, 1993.

[20] Jet Propulsion Laboratory Homepage, Mars Exploration Rover Mission. [Online]. Available: http://marsrovers.jpl.nasa.gov/spotlight/opportunity/b20_20040309.htm

Giulio Reina received the Laurea and Research Doctorate degrees from the Politecnico of Bari, Bari, Italy, in 2000 and 2004, respectively, both in mechanical engineering.

From 2002 to 2003, he worked at the Mobile Robotics Laboratory, University of Michigand as a Visiting Scholar. Currently, he is an Assistant Professor with the Department of Innovation Engineering, University of Lecce, Lecce, Italy. His research interests include ground autonomous vehicles, mobility and localization on rough-terrain, and agricultural robotics.

Lauro Ojeda received the B.S degree in electronic engineering and the M.S. degree in electronics from the Army Polytechnic School, Quito, Ecuador, in 1994 and 1997, respectively.

Currently, he is a Research Investigator at the Mobile Robotics Laboratory, University of Michigan, Ann Arbor. His area of expertise is the development of accurate positioning systems for mobile robots. He has worked on several projects sponsored by DARPA, DOE, and NASA.

Annalisa Milella received the Laurea degree in mechanical engineering (summa cum laude) at the Politecnico di Bari, Bari, Italy, in 2002, where she is pursuing the Research Doctorate degree in mechanical engineering.

In 2005, she was a Visiting Scholar at the EPFL Autonomous Systems Laboratory. Her research interests include autonomous vehicles and computer vision systems. Currently, she is with the Department of Mechanical and Management Engineering, Politecnico di Bari.

Johann Borenstein (M'88–SM'05) received the B.S., M.S., and D.S. degrees from the Technion—Israel Institute of Technology, Haifa, in 1981, 1983, and 1987, respectively, all in mechanical engineering.

Since 1987, he has been a Research Professor and Head of the Mobile Robotics Laboratory, University of Michigan, Ann Arbor. His research interests include mobile robot position estimation and obstacle avoidance, and the design of novel robotic platforms. He has eight patents and over 130 publications on mobile robotics.

Dr. Borenstein was the recipient of the 1998 *Discover* Magazine Award for Technological Innovation in Robotics.